


Characterizing CJPL’s Site-Specific Neutrino Floor as the Neutrino Fog Boundary

Yingjie Fan,^{1,*} Xuewen Liu ^{1,†} and Ning Zhou^{2,‡}

¹*Department of Physics, Yantai University, Yantai 264005, China*

²*Tsung-Dao Lee Institute & School of Physics and Astronomy,
Shanghai Jiao Tong University, Shanghai 201210, China*

The neutrino floor, a theoretical sensitivity limit for Weakly Interacting Massive Particles (WIMPs) in direct dark matter (DM) detection experiments, is redefined as the boundary of a dynamic “neutrino fog”, where neutrino signals become inevitable, obscuring DM detection due to the statistical and systematic uncertainties. This study provides the first site-specific analysis of the neutrino floor at China Jinping Underground Laboratory (CJPL), leveraging its unique geographic and environmental characteristics. We quantify how CJPL’s suppressed atmospheric neutrino flux (around 30% lower than LNGS) reshapes the neutrino floor, thereby enabling improved sensitivity to high-mass WIMPs ($m_{\text{DM}} > 10\text{GeV}$). Using a gradient-based framework, we derive CJPL’s neutrino floor and estimate the detection prospects for the PandaX-xT experiment. Our results demonstrate that a 500 tonne-year exposure with PandaX-xT could touch the floor, probing cross-sections down to $\sigma_{\chi N} \sim 3 \times 10^{-49}\text{cm}^2$.

I. INTRODUCTION

The search for dark matter (DM) has been one of the most significant endeavors in modern physics. Among the various DM candidates, Weakly Interacting Massive Particles (WIMPs) have been a leading hypothesis. Direct detection experiments aim to observe the scattering of WIMPs off atomic nuclei in a detector. However, these experiments face a fundamental challenge in the form of the *neutrino floor*.

The neutrino floor, originally defined as the theoretical sensitivity limit for WIMPs in direct DM detection experiments, has long been regarded as an insurmountable barrier due to irreducible neutrino-induced backgrounds [1]. However, recent advances have revealed that this “floor” is not a static boundary but a dynamic transition zone—termed the *neutrino fog*—where statistical and systematic uncertainties obscure DM signals [2]. This means that the neutrino fog delineates regions of parameter space where WIMP-nucleus interactions become indistinguishable from coherent elastic neutrino-nucleus scattering (CE ν NS) events, primarily sourced from solar (e.g., ^8B), atmospheric, and diffuse supernova neutrino fluxes. The new definition of neutrino fog emphasizes its statistical nature. The transition from Poisson-statistic-dominated to systematic uncertainty-limited regimes is quantified by the gradient index n , where $n = 2$ marks the boundary of the fog (the neutrino floor). For $n > 2$, sensitivity improvements require an exponential increase in exposure, making conventional detection strategies ineffective.

In fact, after numerous years of fruitless searches for DM particles, researchers have first detected a genuine signal emanating from a stream of neutrinos produced by Sun nuclear reactions. Notably, in 2024, the PandaX [3] and XENON [4] collaborations reported that their detectors have likely begun detecting this elusive neutrino fog. Recently, several theoretical studies on this subject also have been conducted, as refer-

enced in [5–10], significantly enhancing our understanding of this irreducible neutrino background.

Critically, the morphology of the neutrino fog exhibits strong geographic dependence, as local neutrino flux variations—modulated by geomagnetic latitude, cosmic-ray modulation, and detector depth—directly influence background kinematics and systematics.

The China Jinping Underground Laboratory (CJPL), with its unique geographic profile (18.06°N geomagnetic latitude, 2400 m rock overburden), presents an exceptional case for studying neutrino fog. Among all existing direct detection experiments, CJPL exhibits the largest crustal geoneutrino flux [11] and the smallest reactor neutrino background [12]. More crucially, the atmospheric neutrino flux at CJPL is notably lower [13], which has a significant impact on the neutrino floor in the high-mass region of DM. Considering these distinctive site-specific attributes, it is imperative to conduct localized fog calculations.

This study delves into two primary questions. Firstly, we examine how the unique neutrino flux characteristics at CJPL alter the landscape of the neutrino fog and floor in comparison to established benchmarks, such as xenon-based detectors located at the Laboratori Nazionali del Gran Sasso (LNGS). Secondly, we calculate the prospective sensitivities and estimate the necessary exposure to touch the neutrino floor in the PandaX experiment conducted at CJPL.

The structure of this paper is outlined as follows. In Section II, we delve into the neutrino fluxes at CJPL. Section III is dedicated to deriving the neutrino floor and fog specific to CJPL. In Section IV, we conduct calculation of the sensitivity of PandaX-xT experiment, aiming to determine the required exposure to reach the new neutrino floor in the high dark matter mass region. Finally, in Section V, we present our conclusions.

II. NEUTRINO FLUXES AT CJPL

The neutrino fluxes, especially those of atmospheric neutrinos, geoneutrinos, and reactor neutrinos, are highly dependent on geographical locations. CJPL is uniquely positioned with

* yingjiefan@s.ytu.edu.cn

† xuewenliu@ytu.edu.cn; corresponding author

‡ nzhou@sjtu.edu.cn; corresponding author

several unparalleled features that distinguish it from other sites. It has the thickest overburden, providing exceptional shielding against cosmic rays, and has the lowest reactor neutrino flux due to its remote location from nuclear power plants [14]. Additionally, CJPL has the largest crustal geoneutrino flux, which is highly advantageous for geoneutrino studies. The laboratory also benefits from the lowest environmental radioactivity, ensuring a cleaner experimental environment, and has the longest solar neutrino path through the Earth, which is particularly beneficial for solar neutrino research. Therefore, the specific geographical and environmental features of CJPL contribute to its specialized neutrino background. We elaborate the pertinent constituents of the neutrino fluxes at CJPL, which are summarised in Fig. 1.

1. Solar neutrino

The Sun produces neutrinos through two primary nuclear reaction chains: the proton-proton (pp) chain and the carbon-nitrogen-oxygen (CNO) cycle. Solar neutrinos dominate the flux at energies $E_\nu \leq 18.77$ MeV [15]. These neutrinos constitute the principal source of CE ν NS events in DM detectors and constrain sensitivity to DM candidates with masses near $m_{\text{DM}} \sim 10$ GeV. Very recently, the PandaX [3] and XENON [4] collaborations independently reported tentative observations of CE ν NS signals.

In this study, we utilize the GS98 high-metallicity Standard Solar Model with the Barcelona 2016 calculations [16]. For all components, we maintain the published normalization uncertainties, with the exception of ^8B , for which a 2% uncertainty was assigned based on comprehensive fits of global neutrino data [17]. Subsequent to ^8B , the ^7Be electron-capture neutrino lines—which are pivotal for enhancing sensitivity to sub-GeV dark matter—are assigned a normalization uncertainty of 6%.

2. Geoneutrinos

Geoneutrinos are antielectron neutrinos released during the decay processes of radioactive isotopes such as uranium (^{238}U), thorium (^{232}Th), and potassium (^{40}K). Their flux directly reflects the radioactive heat production rate and thermal evolution history within the Earth’s interior. The location-dependent geoneutrino flux is particularly sensitive to the amount of crust beneath the laboratory site, which contains the largest portion of heat producing elements. CJPL, situated near the Himalayan mountains in China where the amount of crust is maximal. The uranium and thorium abundances in the local crustal composition significantly influence the spatial distribution of the geoneutrino flux in this region. This has been previously identified as a favorable location for geoneutrino detection [11].

For concreteness, we use geoneutrino flux from Ref. [18], with corresponding uncertainties for each component.

3. Reactor neutrinos

This is another source of antineutrinos and influence the background at slightly higher masses. Jinping is far away from all the nuclear power plants [14] in operation and under construction.

The reactor neutrino background at Jinping is the lowest among all the direct detection experiments. The total differential reactor neutrino flux at Jinping is employed from Ref. [12].

4. The diffuse supernova neutrino background (DSNB)

DSNB is a relic flux of neutrinos and antineutrinos from core-collapse supernovae in cosmic history—emerges as a critical astrophysical background for DM direct detection. For DM experiments, the DSNB-induced CE ν NS creates an irreducible “neutrino floor” near $m_\chi \sim 20$ GeV. A 50% uncertainty on the all-flavor flux accounts for cosmic variance in supernova rates, progenitor mass-dependent spectral ambiguities, and neutrino oscillation effects [19]. We use the same flux as in Ref. [2].

5. Atmospheric neutrinos

Atmospheric neutrinos exhibit significant geographic dependence due to variations in cosmic ray flux, Earth’s geometry, and magnetic field effects. At high latitudes (e.g., polar regions), weaker geomagnetic shielding results in higher cosmic ray flux and neutrino production, while low latitudes (e.g., equatorial regions) experience reduced flux due to stronger magnetic deflection.

CJPL is situated in a geomagnetic low-latitude region (with a geomagnetic latitude of 18.06°N), where the atmospheric neutrino flux is predominantly driven by higher-energy cosmic rays. The flux at CJPL undergoes suppression in comparison to LNGS, primarily due to the combination of a relatively high rigidity cutoff energy and the exceptional cosmic-ray shielding afforded by Jinping Mountain.

The atmospheric flux used in this work is the average of the solar min and solar max flux calculated in [13], with placing the recommended 25% theoretical uncertainty.

III. NEUTRINO FLOOR AND FOG FOR CJPL

In this section, we initially revisit the newly introduced definition of the neutrino floor, as presented in Ref. [2]. Subsequently, we derive our novel neutrino floor specifically for CJPL. For the sake of completeness, the scattering rates pertaining to dark matter-nuclear scattering and CE ν NS are provided in Sec. IV and Appendix A, respectively.

A. Statistical Methods and Sensitivity Evolution

The neutrino fog refers to the obscured region in direct DM detection experiments where the neutrino background

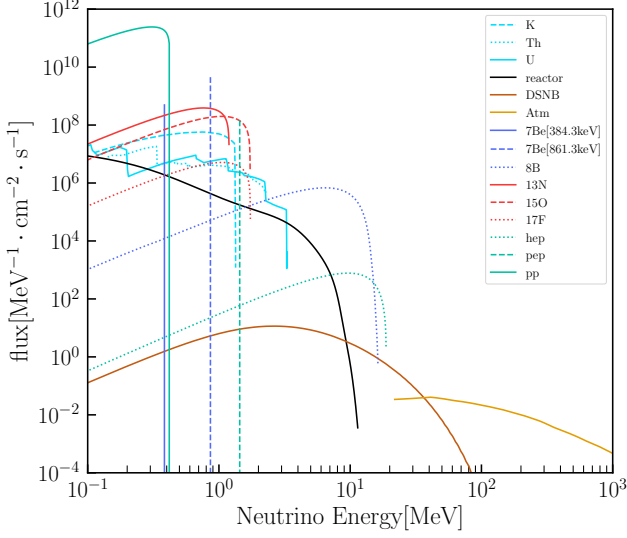


Figure 1. Neutrino fluxes at CJPL. Fluxes from different neutrino sources are shown with different colors: geoneutrinos are light blue, neutrinos from reactors is shown with black, lines with purple are solar neutrinos, DSNB neutrinos are shown with brown, and atmospheric neutrinos is shown with orange.

and the DM signal energy spectra overlap significantly, rendering them indistinguishable. This phenomenon leads to a stagnation in experimental sensitivity. The underlying mechanism arises when the dark matter signal strength falls below the combined effects of systematic uncertainties and statistical fluctuations of the neutrino background, thereby masking the signal entirely. The neutrino floor, defined as the dynamical boundary of the neutrino fog, represents the critical hypersurface in parameter space where a dark matter signal transitions from a detectable regime to an indistinguishable one. This boundary is not static but evolves dynamically with experimental statistics, systematic errors, and target material properties.

The statistical inference employs a binned likelihood function, incorporating Poissonian probabilities and Gaussian distributions to model background interference:

$$\mathcal{L}(\sigma, \Phi) = \prod_{i=1}^{N_{\text{bins}}} \mathcal{P} \left[N_{\text{obs}}^i | N_{\chi}^i + \sum_{j=1}^{n_{\nu}} N_{\nu}^i(\Phi^j) \right] \prod_{j=1}^{n_{\nu}} \mathcal{G}(\Phi^j), \quad (1)$$

where the Poissonian term describes the statistical fluctuations between the observed event number N_i^{obs} and the expected signal events N_i^{exp} in each energy bin. The Gaussian term introduces neutrino flux normalization parameters Φ_j , which are considered as the nuisance parameters, with standard deviations $\delta\Phi$ quantifying systematic uncertainties in flux calculations. Parameters are the DM mass and cross section.

Hypothesis testing compares the null background-only model ($\mathcal{M}_{\sigma=0}$) against the signal-plus-background model

(\mathcal{M}). A discovery threshold of $q_0 > 9$ (corresponding to 3σ significance) defines the exclusion limit [2]:

$$q_0 = \begin{cases} -2 \ln \left[\frac{\mathcal{L}(0, \hat{\Phi} | \mathcal{M}_{\sigma=0})}{\mathcal{L}(\hat{\sigma}, \hat{\Phi} | \mathcal{M})} \right] & \hat{\sigma} > 0 \\ 0 & \hat{\sigma} \leq 0 \end{cases} \quad (2)$$

where \mathcal{L} is maximised at $\hat{\Phi}$ when σ is set to 0, and $(\hat{\sigma}, \hat{\Phi})$ when σ is a free parameter. The model $\mathcal{M}_{\sigma=0}$ is a special case of \mathcal{M} , obtained by fixing one parameter to the boundary of its allowed space. Therefore Chernoff's theorem holds [20], and q_0 should be asymptotically distributed according to $\frac{1}{2}\chi_1^2 + \frac{1}{2}\delta(0)$ when \mathcal{M} is true [21].

The sensitivity evolution as a function of N (the number of observed background events) exhibits three distinct regimes[2]: (a) background independent regime ($N \ll 1$). The sensitivity scales as $\sigma \propto N^{-1}$, where background fluctuations are negligible. (b) Poisson statistic dominated regime ($N \gg 1$). The sensitivity follows $\sigma \propto N^{-1/2}$, governed by statistical fluctuations. (c) systematics uncertainty dominated regime ($N \geq 1/\delta\Phi^2$). The sensitivity stagnates as $\sigma \propto \sqrt{1 + N\delta\Phi^2/N}$, where systematic errors dominate [1].

With these features, resulting the mathematical characterization of the neutrino fog, known as the ‘opacity’, which is defined by the gradient index:

$$n = - \left(\frac{d \log \sigma}{d \log N} \right)^{-1} \quad (3)$$

For $n = 2$ (Poisson statistic dominated regime), the sensitivity adheres to $\sigma \propto N^{-1/2}$. When $n > 2$ (systematics uncertainty dominated regime), the experiment enters the neutrino fog's saturation phase, where sensitivity plateaus.

By mapping the $n = 2$ contour, the neutrino floor is identified as the critical hypersurface in the dark matter mass m_{χ} and cross-section σ parameter space where sensitivity degradation becomes irreversible.

B. Neutrino floor for CJPL

Building upon the public code [22] developed by O'Hare, this study pioneers the integration of neutrino flux data from CJPL to derive geographically characterized neutrino floor curves, as shown in Fig. 2. The comparative analysis reveals key findings through following comparisons.

For the location effects, in the high-mass region (WIMP mass > 10 GeV), CJPL's neutrino floor demonstrates a 30% lower background limit compared to LNGS, marked by the black dotted curve. This advantage stems from CJPL's unique geological profile: Its atmospheric neutrino flux is reduced by approximately (20–40)% relative to LNGS, attributable to enhanced cosmic-ray shielding by the Jinping Mountain and its lower geomagnetic latitude. Consequently, high-energy nuclear recoil backgrounds—dominant in this mass range—are

suppressed. Future research should aim to optimize the treatment of atmospheric neutrinos to improve the accuracy of neutrino background limits.

In the realm below 10 GeV, the neutrino floors at CJPL and LNGS display a striking degree of consistency. This convergence is primarily attributed to the dominance of solar neutrinos, which contribute an impressive 90% to the overall neutrino flux, with minimal variations observed across different geographical locations. Although the crustal geoneutrino flux at CJPL is notably higher than that at LNGS—a disparity linked to regional variations in uranium and thorium concentrations—the impact of geoneutrinos in the low-mass region is rendered negligible.

When compared to the neutrino floor derived from traditional techniques by Ref. [1] (depicted as the light brown line), the fog boundary at CJPL exhibits significant deviations across the entire mass range. These deviations arise from similar underlying factors as those influencing the neutrino floor at LNGS, as discussed in detail in Ref. [2].

To visualize the neutrino fog, the color-mapping technique across the DM parameter space based on the gradient index n is implemented. This methodology is demonstrated in Fig. 2, where the color scale above the plot explicitly indicates the n -value for each point within the fog.

The opacity of the neutrino fog quantifies the resistance to experimental progress through the parameter space, revealing regions where overlapping neutrino backgrounds obscure DM discovery. This metric highlights zones where spectral degeneracies between DM and neutrino-induced recoils are most pronounced. Darker regions in Fig. 2 correspond to $n > 2$, signifying enhanced spectral degeneracy where DM and neutrino event rates become nearly indistinguishable.

While subtle differences between DM and neutrino signals persist in most scenarios, these distinctions can be statistically resolved in high-exposure regimes. Notably, once the accumulated event count N surpasses a critical threshold, the sensitivity scaling reverts to $n = 2$ for extremely low cross-sections, reflecting a transition back to Poisson-statistics-dominated sensitivity.

A comparison reveals distinct characteristics between the neutrino fog at CJPL and LNGS. These differences stem from site-specific variations in neutrino flux components and their associated systematic uncertainties. Such geographic disparities underscore the necessity of site-specific fog modeling to optimize future DM detection strategies.

IV. EXPERIMENTAL SENSITIVITY OF PANDAX-XT

Given the establishment of the new neutrino floor at CJPL, it is crucial to explore the potential detection prospects by the PandaX experiment.

We undertake an estimate of the direct detection capabilities using the PandaX-xT experiment at CJPL [24], focusing on a liquid xenon detector with a mass of 40 tonnes. Our calculation assumes a duration of exposure spanning several years, as detailed in [24].

In this work, we focus on the standard spin-independent

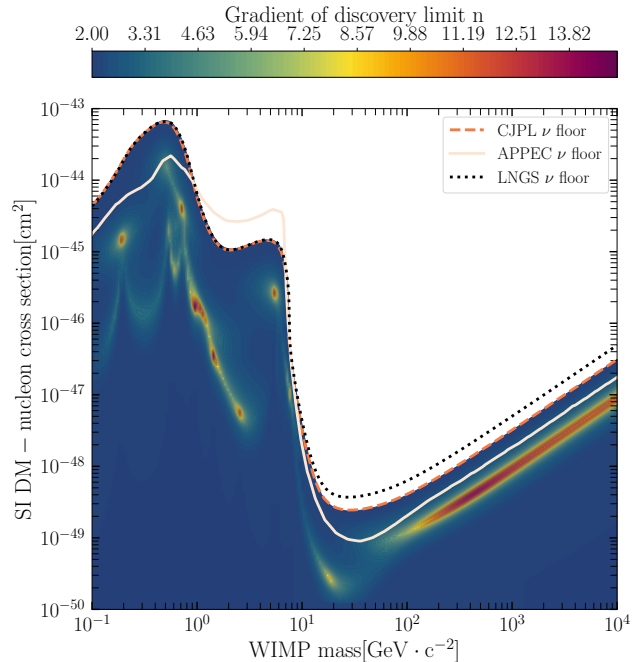


Figure 2. Neutrino floor and fog for CJPL. The red dashed curve represents the neutrino floor as the boundary for neutrino fog with $n = 2$ in this work, the black dotted line is the neutrino floor at LNGS with $n = 2$ calculated in Ref. [2], neutrino floor shown by the light brown line is APPEC adopted [23] (based on the technique of Ref. [1]). The color scale shows the value of n .

(SI) interactions and consider only elastic scattering. The scattering rate is the same as the detection rate and can be expressed as [25]:

$$\frac{dR}{dE_R}(E_R, t) = \sigma_p \frac{\rho}{m_{\text{DM}}} \frac{1}{2\mu_N^2} \sum_T \zeta_T [Z + (A - Z) f_n/f_p]^2 \times F_{SI}^2(E_R) \eta_0(v_{\min}(E_R), t), \quad (4)$$

which is the scattering rate summed over all target nuclides. σ_p is the WIMP-proton cross-section, in this work, we use $\rho = 0.3 \text{ GeV/cm}^3$ for the local dark matter density, μ_N is the reduced mass of the WIMP-nucleus system, ζ_T is the mass fraction of the isotope T in the detector, Z is the atomic number of the target nucleus, A is the atomic mass number of the target nucleus, and f_n/f_p is the ratio between the neutron and proton couplings to the WIMP. For the standard assumption in this work, we take $f_p = f_n$, to ensure that the DM-proton and DM-neutron couplings are the isosinglet. $F_{SI}^2(E_R)$ is taken to be the Helm form factor in this work [26]. $\eta_0(v_{\min}(E_R), t)$ represents the velocity distribution of the DM particles.

To properly reproduce the event rate measured by the experiments, we need to take into account the detection efficiency,

the total number of events is given by:

$$N \approx \text{exposure} \times \int_0^\infty dE_R \frac{dR}{dE_R} \epsilon(E_R). \quad (5)$$

Here, $\epsilon(E_R)$ is the detection efficiency, we use the efficiency curve of the current PandaX-4T detector [27], which covers the energy range from approximately 4 to 110 keV. To ensure the completeness of all detectable events, we set the upper limit of the energy window at a sufficiently large value, covering the maximum energy range that the experiment can detect.

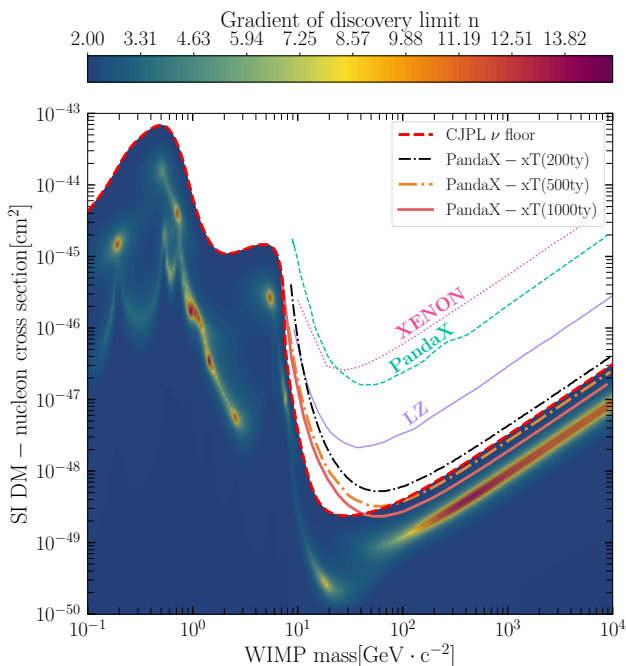


Figure 3. Sensitivity and neutrino background. The latest excluded limits are shown with purple solid line for LZ [28], PandaX4T [29] with green dashed line and XENONnT [30] with magenta dotted line. The prospective sensitivities are also shown in this figure, the black dash-dotted line is the prospect from PandaXnT with a 200 tonne-year exposure which is consisted with Ref. [24], orange dash dotted line and pink solid line corresponding to the sensitivity for a 500 tonne-year and 1000 tonne-year exposure at PandaX-xT experiment respectively.

Based on the aforementioned statistical methods, the likelihood function is modified as follows to perform the detection simulation:

$$\mathcal{L}(\sigma, \Phi) = \prod_{i=1}^{N_{\text{bins}}} \mathcal{P} \left[N_{\text{obs}}^i | N_{\chi}^i + \sum_{j=1}^{n_{\nu}} n_{\nu}^i(\Phi^j) + n_{\text{bkg}}^i \right] \times \prod_{j=1}^{n_{\nu}} \mathcal{G}(\Phi^j) \mathcal{G}(n) \quad (6)$$

where n_{bkg}^i represents the background events in the PandaX detector, following the results reported in [24]. Additionally, we assume that the background events are uniformly distributed within the detector. It should be noted that we have updated the neutrino nuclear recoil background event rate using our calculated results for the front part of this work.

Applying the likelihood ratio test (Eq. 2), the projected 90% confidence level exclusion sensitivity reaches of the PandaX-xT experiment are shown in Figure 3. For benchmark validation, we initially compute the sensitivity curve at 200 tonne-years (ty) exposure (black dot-dashed line), which shows well consistency with the PandaX Collaboration’s baseline simulations [24]. This agreement confirms the validity of our treatment. The the orange dot-dashed curve and the pink solid curve are the sensitivities with 500ty, and 1000ty exposures respectively.

Our results show almost no improvement in the region of WIMP mass smaller than 10 GeV/c² among all the curves, this is due to the lower efficiency in this region. In future detections, the PandaX-xT experiment is expected to achieve a more improvement in detection sensitivity in the lower mass region, specially it will provide more accurate results for ⁸B solar neutrinos region.

Our central finding reveals that penetrating the neutrino floor requires accumulated exposures exceeding 500 tonne-years for WIMP masses above 10 GeV (see the orange dotted curve). At this threshold, PandaX-xT’s sensitivity approaches cross-sections of $\sigma_{\chi N} \sim 3 \times 10^{-49}$ cm² at a WIMP mass of 40 GeV/c², marking the onset of neutrino floor dominance. We further present the results for a 1000 tonne-years exposure. In the “saturation region” of the neutrino fog, systematic uncertainties—such as those associated with the calculation of the neutrino flux—become the dominant factors. Consequently, the experimental sensitivity cannot be effectively improved with increasing exposure.

V. CONCLUSION

This study presents the first site-specific characterization of the neutrino floor and fog at CJPL, driven by its unique geographic and environmental conditions. By integrating the suppressed atmospheric neutrino flux of CJPL (~ 30% lower than LNGS) and the enhanced geoneutrino contributions into a gradient-based statistical framework, we redefine the neutrino fog boundary as a dynamic transition zone governed by Poisson-statistical and systematic uncertainties. These features reduce the neutrino floor by nearly 30% for high-mass WIMPs ($m_{\text{DM}} > 10$ GeV), enhancing sensitivity through reduced neutrino backgrounds. Below 10 GeV, solar neutrino

dominance homogenizes sensitivity limits across sites. The sensitivity estimation of the PandaX-xT experiment shows that a 500 tonne-year exposure reaches cross-sections as low as $\sigma_{\chi N} \sim 3 \times 10^{-49} \text{ cm}^2$, intersecting CJPL's neutrino floor. Critical challenges persist, particularly systematic uncertainties in neutrino flux normalization, underscoring the need for refined models and multi-detector synergies.

ACKNOWLEDGMENTS

The work by X.L. is supported by the Project of Shandong Province Higher Educational Science and Technology Program under Grants No. 2022KJ271. The work by N.Z. is supported by National Science Foundation of China (No. 12325505).

Appendix A: Scattering rate for CE ν NS

Neutrinos can scatter elastically off nuclei and produce recoils with very similar spectra to the ones found by DM-nucleus scattering. Currently, the only measurement of CE ν NS is by COHERENT [31, 32], but it is well-understood in the Standard Model [33, 34]. Similar to the WIMP event

rate calculation, the neutrino event rate is computed by the convolution of the differential CE ν NS cross section and the neutrino flux,

$$\frac{dR_\nu}{dE_r} = \frac{1}{m_N} \int_{E_\nu^{\min}} \frac{d\Phi}{dE_\nu} \frac{d\sigma_{\nu N}(E_\nu)}{dE_r} dE_r, \quad (\text{A1})$$

here we cut off the integral at the minimum neutrino energy that can cause a recoil with E_r : $E_\nu^{\min} = \sqrt{m_N E_r}/2$. The differential neutrino-nucleus cross section as a function of the recoil energy and the neutrino energy is given by Refs. [1, 35–37],

$$\frac{d\sigma(E_\nu, E_r)}{dE_r} = \frac{G_f^2}{4\pi} Q_\omega^2 m_N \left(1 - \frac{m_N E_r}{2E_\nu^2}\right) F_{SI}^2(E_r), \quad (\text{A2})$$

where m_N is the nucleus mass, G_f is the Fermi coupling constant and $Q_\omega = N - (1 - 4\sin^2\theta_\omega)Z$ is the weak nuclear hypercharge with N the number of neutrons, Z the number of protons, and θ_ω the weak mixing angle, taking $\sin^2\theta_\omega = 0.2387$. The presence of the form factors describes the loss of coherence at higher momentum transfer and is assumed to be the same as for the WIMP-nucleus SI scattering, for which we use the standard Helm form factor [38].

-
- [1] J. Billard, L. Strigari, and E. Figueroa-Feliciano, *Phys. Rev. D* **89**, 023524 (2014), arXiv:1307.5458 [hep-ph].
- [2] C. A. J. O'Hare, *Phys. Rev. Lett.* **127**, 251802 (2021), arXiv:2109.03116 [hep-ph].
- [3] Z. Bo *et al.* (PandaX), *Phys. Rev. Lett.* **133**, 191001 (2024), arXiv:2407.10892 [hep-ex].
- [4] E. Aprile *et al.* (XENON), *Phys. Rev. Lett.* **133**, 191002 (2024), arXiv:2408.02877 [nucl-ex].
- [5] J. Tang and B.-L. Zhang, *Phys. Rev. D* **108**, 062004 (2023), arXiv:2304.13665 [hep-ph].
- [6] B. Carew, A. R. Caddell, T. N. Maity, and C. A. J. O'Hare, *Phys. Rev. D* **109**, 083016 (2024), arXiv:2312.04303 [hep-ph].
- [7] J. Tang and B.-L. Zhang, *JHEP* **12**, 074 (2024), arXiv:2403.05819 [hep-ph].
- [8] I. M. Bloch, S. Bottaro, D. Redigolo, and L. Vittorio, (2024), arXiv:2410.02723 [hep-ph].
- [9] P. Blanco-Mas, P. Coloma, G. Herrera, P. Huber, J. Kopp, I. M. Shoemaker, and Z. Tabrizi, (2024), arXiv:2411.14206 [hep-ph].
- [10] T. N. Maity, (2024), arXiv:2412.17649 [hep-ph].
- [11] L. Wan, G. Hussain, Z. Wang, and S. Chen, *Phys. Rev. D* **95**, 053001 (2017), arXiv:1612.00133 [hep-ex].
- [12] J. F. Beacom *et al.* (Jinping), *Chin. Phys. C* **41**, 023002 (2017), arXiv:1602.01733 [physics.ins-det].
- [13] Y. Zhuang, L. E. Strigari, and R. F. Lang, *Phys. Rev. D* **105**, 043001 (2022), arXiv:2110.14723 [hep-ph].
- [14] International Atomic Energy Agency, "http://www.iaea.org/" (2015).
- [15] E. G. Adelberger *et al.*, *Rev. Mod. Phys.* **83**, 195 (2011), arXiv:1004.2318 [nucl-ex].
- [16] N. Vinyoles, A. M. Serenelli, F. L. Villante, S. Basu, J. Bergström, M. C. Gonzalez-Garcia, M. Maltoni, C. Peña Garay, and N. Song, *Astrophys. J.* **835**, 202 (2017), arXiv:1611.09867 [astro-ph.SR].
- [17] J. Bergstrom, M. C. Gonzalez-Garcia, M. Maltoni, C. Pena-Garay, A. M. Serenelli, and N. Song, *JHEP* **03**, 132 (2016), arXiv:1601.00972 [hep-ph].
- [18] G. B. Gelmini, V. Takhistov, and S. J. Witte, *Phys. Rev. D* **99**, 093009 (2019), arXiv:1812.05550 [hep-ph].
- [19] J. F. Beacom, *Ann. Rev. Nucl. Part. Sci.* **60**, 439 (2010), arXiv:1004.3311 [astro-ph.HE].
- [20] H. Chernoff, *Ann. Math. Stat.* **25**, 573 (1954).
- [21] S. Algeri, J. Aalbers, K. Dundas Morà, and J. Conrad, *Nature Rev. Phys.* **2**, 245 (2020), arXiv:1911.10237 [physics.data-an].
- [22] O'Hare, "NeutrinoFog,".
- [23] J. Billard *et al.*, *Rept. Prog. Phys.* **85**, 056201 (2022), arXiv:2104.07634 [hep-ex].
- [24] A. Abdurkirim *et al.* (PANDA-X, PandaX), *Sci. China Phys. Mech. Astron.* **68**, 221011 (2025), arXiv:2402.03596 [hep-ex].
- [25] E. Del Nobile, *Lect. Notes Phys.* **996** (2022), 10.1007/978-3-030-95228-0, arXiv:2104.12785 [hep-ph].
- [26] R. H. Helm, *Phys. Rev.* **104**, 1466 (1956).
- [27] Y. Meng *et al.* (PandaX-4T), *Phys. Rev. Lett.* **127**, 261802 (2021), arXiv:2107.13438 [hep-ex].
- [28] J. Aalbers *et al.* (LZ), (2024), arXiv:2410.17036 [hep-ex].
- [29] Z. Bo *et al.* (PandaX), *Phys. Rev. Lett.* **134**, 011805 (2025), arXiv:2408.00664 [hep-ex].
- [30] E. Aprile *et al.* (XENON), *Phys. Rev. Lett.* **131**, 041003 (2023), arXiv:2303.14729 [hep-ex].
- [31] D. Akimov *et al.* (COHERENT), *Science* **357**, 1123 (2017), arXiv:1708.01294 [nucl-ex].
- [32] D. Akimov *et al.* (COHERENT), *Phys. Rev. Lett.* **126**, 012002 (2021), arXiv:2003.10630 [nucl-ex].
- [33] D. Z. Freedman, *Phys. Rev. D* **9**, 1389 (1974).

- [34] D. Z. Freedman, D. N. Schramm, and D. L. Tubbs, *Ann. Rev. Nucl. Part. Sci.* **27**, 167 (1977).
- [35] K. Scholberg, *Phys. Rev. D* **73**, 033005 (2006), [arXiv:hep-ex/0511042](#).
- [36] F. Ruppin, J. Billard, E. Figueroa-Feliciano, and L. Strigari, *Phys. Rev. D* **90**, 083510 (2014), [arXiv:1408.3581 \[hep-ph\]](#).
- [37] C. A. J. O'Hare, *Phys. Rev. D* **102**, 063024 (2020), [arXiv:2002.07499 \[astro-ph.CO\]](#).
- [38] J. D. Lewin and P. F. Smith, *Astropart. Phys.* **6**, 87 (1996).